

Transferable Learning of Reaction Pathways from Geometric Priors

Juno Nam,^{†,‡} Miguel Steiner,[†] Max Misterka,[¶] Soojung Yang,[§] Avni Singhal,[†] and Rafael Gómez-Bombarelli^{*,†}

[†]*Department of Materials Science and Engineering, Massachusetts Institute of Technology, Cambridge, Massachusetts 02139, United States*

[‡]*Energy Storage Research Alliance, Argonne National Laboratory, 9700 South Cass Avenue, Lemont, Illinois 60439, United States*

[¶]*Department of Mathematics, Massachusetts Institute of Technology, Cambridge, Massachusetts 02139, United States*

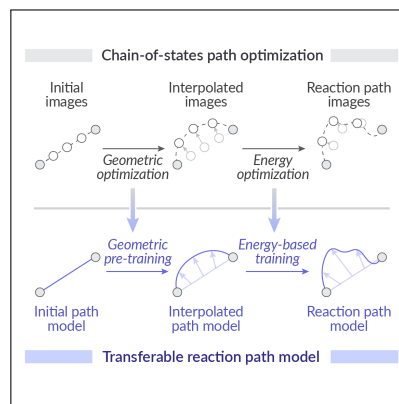
[§]*Computational and Systems Biology Program, Massachusetts Institute of Technology, Cambridge, Massachusetts 02139, United States*

E-mail: rafagb@mit.edu

Abstract

Identifying minimum-energy paths (MEPs) is crucial for understanding chemical reaction mechanisms but remains computationally demanding. We introduce MEPIN, a scalable machine-learning method for efficiently predicting MEPs from reactant and product configurations, without relying on transition-state geometries or pre-optimized reaction paths during training. The task is defined as predicting deviations from geometric interpolations along reaction coordinates. We address this task with a continuous reaction path model based on a symmetry-broken equivariant neural network that generates a flexible number of intermediate structures. The model is trained using an energy-based objective, with efficiency enhanced by incorporating geometric priors from geodesic interpolation as initial interpolations or pre-training objectives. Our approach generalizes across diverse chemical reactions and achieves accurate alignment with reference intrinsic reaction coordinates, as demonstrated on various small molecule reactions and [3+2] cycloadditions. Our method enables the exploration of large chemical reaction spaces with efficient, data-driven predictions of reaction pathways.

TOC Graphic



Introduction Uncovering atomistic chemical reaction pathways enables the reliable prediction of properties such as reaction rates and product distributions that can accelerate various process optimization tasks. A key step in this process is identifying the minimum energy path (MEP), which links reactants and products via the transition state (TS). Conventional methods for locating MEPs, including the nudged elastic band (NEB) method^{1,2} and other chain-of-states techniques—which generate a series of intermediate configurations (or “images”) between reactant and product states—require extensive energy and force evaluations, typically at the density functional theory (DFT) level. Additionally, standard optimization procedures often suffer from issues such as kinks, corner-cutting, and sliding,^{3,4} as well as oscillations leading to poor convergence⁵. As a result, these methods are computationally intensive and are unsuitable for large-scale reaction discovery across diverse chemical spaces.

Machine learning (ML) methods have been introduced to accelerate reaction path calculations and bypass the challenges of chain-of-states optimization. A common approach is to replace expensive DFT energy and force evaluations with more efficient surrogate reactive ML interatomic potentials (MLIPs)^{6,7}, often referred to as the “neural NEB” method^{8–12}. While these models significantly reduce computational costs compared to explicit quantum mechanical calculations, training reliable reactive MLIPs requires datasets of transition-region configurations, ideally sampled near the low-energy path. This creates a “chicken-and-egg” problem: transition path sampling is needed to generate training data, yet the reactive MLIPs are intended to enable such sampling. One potential solution is to use active learning strategies to improve an MLIP through iterative molecular dynamics simulations^{13–21}. However, these strategies have only been demonstrated for individual systems, lack transferability to other reactions, and require substantial reference data. They also rely on defining a reaction coordinate to accelerate simulations, which demands expert intuition and detailed knowledge of the reaction mechanism. Another ML-based approach avoids conventional MEP optimizations and instead directly predicts the TS structure from the reactant and product structures.^{22–26} At inference, this method is typically much faster than neural NEB approaches as it avoids structure optimizations. However, the training of such a method still relies on a dataset

of pre-optimized TS structures on the potential energy surface of interest, and such datasets remain limited in both size and chemical diversity.²⁶

To address the common limitation of requiring transition pathway or structure data to model the same, we propose an alternative paradigm based on implicit parametrization of reaction pathways. Several recent works have demonstrated that neural representations of reaction pathways, either explicitly coupled with dynamics in transition path sampling^{27–31} or used as parametrized approximations of the MEP^{32–34}, can be effective for reaction path searches within individual systems of interest. Applications in chemical reaction path finding have shown that continuous parametrization effectively resolves the previously mentioned issues associated with NEB optimization³³. However, these approaches are typically not designed to generalize across systems. Here, we extend this idea to develop a chemically transferable model of a parametrized reaction path, MEPIN (MEP Inference Network), that can be trained using only reactant and product configurations along with energy and force evaluations, and then can be directly applied to unseen reactions at inference time without energy or force evaluations. As illustrated in Fig. 1, parametrizing the path itself eliminates the need for pre-computed transition data by generating the required information on the fly in the training process. This removes reliance on prior transition knowledge, such as successfully optimized structures or paths, and enables a scalable and transferable framework for reaction path discovery.

Parametrization of reaction path Given the reactant configuration $x_R \in \mathbb{R}^{N \times 3}$ and product configuration $x_P \in \mathbb{R}^{N \times 3}$, each with N atoms in the same index ordering, and elemental identities $a \in \mathcal{A}^N$ from a set of elements \mathcal{A} , we define a reaction path model $f(x_R, x_P, a, t; \theta)$ that represents the MEP between them as a function of reaction progress $t \in [0, 1]$:

$$f(x_R, x_P, a, t; \theta) = f_{\text{interp}}(x_R, x_P, a, t) + t(1 - t)\phi(x_R, x_P, a, t; \theta), \quad (1)$$

where ϕ is a neural network model with parameters θ that predicts the deviation from the initial interpolation f_{interp} to the true MEP. f_{interp} can be any interpolation that depends only on x_R and x_P , such as a linear interpolation $(1 - t)x_R + tx_P$ or a geodesic interpolation, as shown later. We refer to the models as MEPIN-**L** and MEPIN-**G**, re-

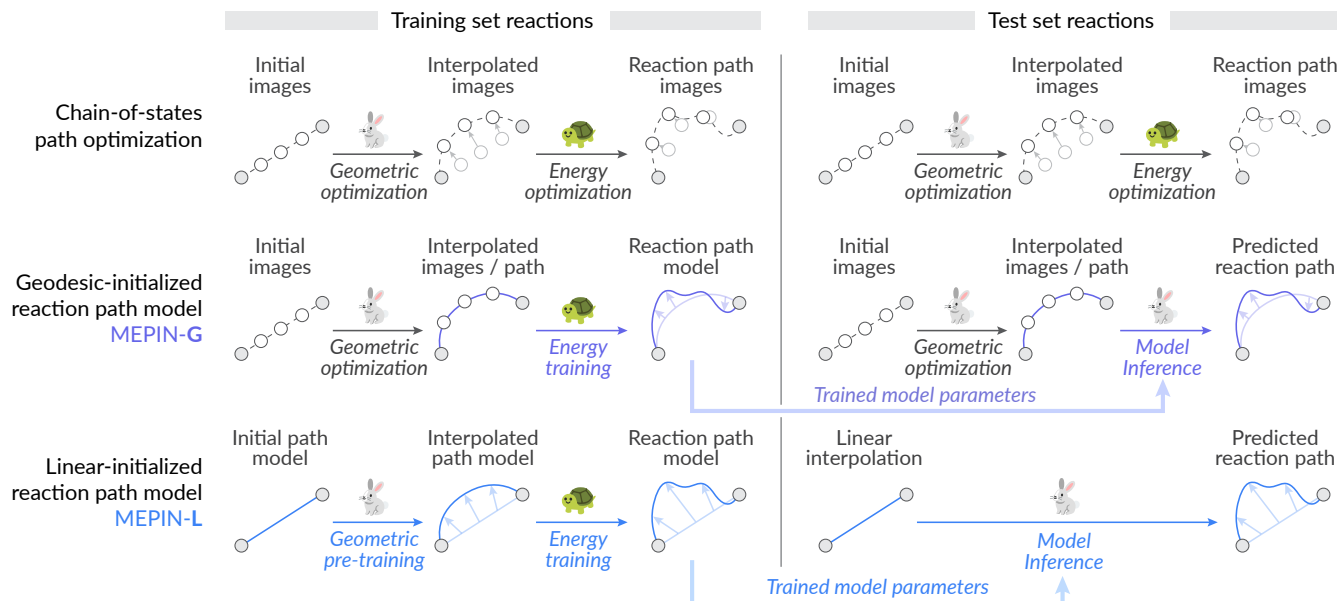


Figure 1: Schematic of the MEPIN (MEP Inference Network) training and inference. The model leverages an implicit reaction path parametrized by a neural network to transfer knowledge of the reaction path learned during training to unseen reactant-product pairs. It learns the difference between the minimum energy path and initial interpolation, derived from either geodesic (MEPIN-G) or linear (MEPIN-L) interpolations. The linear-initialized model may also benefit from geometric pre-training on geodesic interpolation. The proposed approach speeds up reaction path finding by reducing the need for costly energy evaluations at inference time.

spectively (see Fig. 1). We explicitly parametrize the model based on the geometries and elemental identities of the reactants and products to enable chemical transferability. In all experiments, x_R and x_P were translationally and rotationally aligned to minimize the root mean square deviation (RMSD). During training, the product structures are optionally augmented by small rotations to enhance robustness (see the Supporting Information).

We implement ϕ as a message-passing equivariant graph neural network, adapted from the PaiNN architecture³⁵. The input atomic graph is constructed with atoms as nodes and edges connecting atoms within a cutoff distance in either x_R or x_P . The node features encode elemental identities and the edge features are derived from interatomic distances and orientations of x_R , x_P , and the interpolated geometry $f_{\text{interp}}(x_R, x_P, a, t)$.

Message passing schemes for atomistic systems are typically constructed to preserve the physical symmetries of the potential energy function through E(3)-equivariance. For the reaction path in Eq. (1), this implies that a group operation $g \in E(3)$ transforms the path in the same way as the endpoint geometries: $f(g \circ x_R, g \circ x_P, a, t; \theta) = g \circ f(x_R, x_P, a, t; \theta)$. However, even if the underlying

potential energy is symmetric under a group, the MEP may exhibit reduced symmetries³⁶. For example, consider a two-dimensional potential shown in Fig. 2a, where the potential energy, configurations x_R and x_P , and their linear interpolants are all symmetric with respect to the mirror plane σ . If the true path is asymmetric, as shown in Fig. 2a, an E(3)-equivariant model cannot reproduce this asymmetry from symmetric inputs, as its outputs are inherently constrained to maintain planar symmetry:

$$\begin{aligned} \sigma \circ \phi(x_R, x_P, a, t) &= \phi(\sigma \circ x_R, \sigma \circ x_P, a, t) \\ &= \phi(x_R, x_P, a, t). \end{aligned} \quad (2)$$

For example, in the reaction shown in Fig. 2b from the Transition1x set³⁷, the planar molecule temporarily adopts a non-planar geometry as a hydrogen atom shifts out of the ring plane during the reaction. An E(3)-equivariant path model cannot capture such asymmetric displacements, resulting in a strictly planar reaction path (Fig. 2c). To address this, we intentionally break the parity symmetry in our model. Specifically, we adopt the message passing scheme from Schreiner et al.³⁸, which incorporates vector products to enable chiral vector predictions, making the model SE(3)-

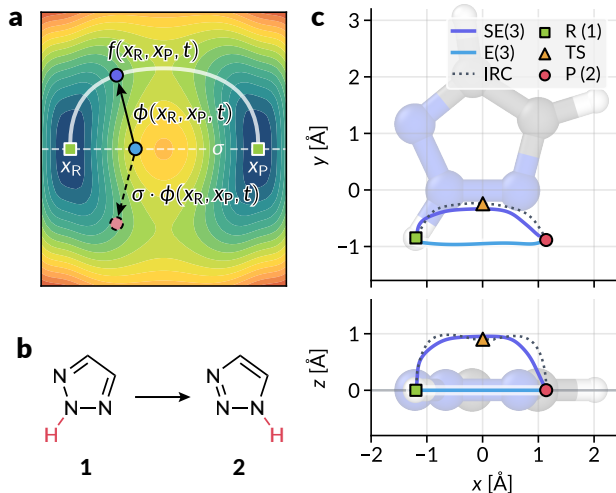


Figure 2: Symmetry considerations for the reaction path model. (a) Two-dimensional example showing a symmetric potential landscape and linear interpolation path with respect to reflection σ , while the MEP is asymmetric. The NN model ϕ , which learns the deviation between the initial interpolation and the MEP (scale factor $t(1-t)$ and argument a are omitted), must be non-equivariant with respect to σ to properly break the symmetry. (b) Conversion between triazole tautomers **1** and **2**. (c) Projections of the intrinsic reaction coordinates (IRCs) and reaction paths on the x - y and x - z planes learned by an SE(3)- and E(3)-equivariant neural networks for the reaction shown in panel (b). Curves and markers denote the positions of migrating hydrogen atoms, with the ring atoms aligned. The E(3) model fails to capture the out-of-plane atomic displacement.

equivariant rather than E(3)-equivariant. We note that while symmetry-breaking requirements may vary with the reactants, this approach can be generalized, with arbitrary symmetry reduction incorporated into the network via symmetry breaking sets³⁹. Additional details on the model architecture are reported in the Supporting Information.

Energy-based training objective Given the parametrized reaction path model Eq. (1), we introduce an energy-based objective to optimize the parameters so that the predicted path is aligned with the unknown true MEP during training. We leverage the variational formulation of the MEP based on the maximum reactive flux formalism^{40,41}. For a potential energy function $U : \mathbb{R}^{N \times 3} \rightarrow \mathbb{R}$, which implicitly depends on elemental identities a , and an arbitrary reaction path $x :$

$[0, 1] \rightarrow \mathbb{R}^{N \times 3}$ connecting the reactant $x_R = x(0)$ and product $x_P = x(1)$ configurations, the reactive flux under overdamped Langevin dynamics is inversely proportional to the following path functional:

$$\mathcal{L}_{\text{flux}}[x(t)] = \frac{1}{\beta} \log \int_0^1 \exp(\beta U(x(t))) \|\dot{x}(t)\| dt, \quad (3)$$

where $\beta = 1/k_B T$ is the inverse temperature. Notably, in the zero-temperature limit ($\beta \rightarrow \infty$), the path minimizing Eq. (3) (maximizing the flux) coincides with the MEP:

$$x_{\text{MEP}}(t) = \lim_{\beta \rightarrow \infty} \arg \min_{x(t)} \mathcal{L}_{\text{flux}}[x(t)]. \quad (4)$$

Thus, the MEP can be approximated by optimizing Eq. (3) at sufficiently large but numerically feasible β ; in this work, we used $\beta = 20 \text{ eV}^{-1}$. This method, also known as the MaxFlux approach, has been successfully applied in reaction path finding using chain-of-states representation, demonstrating improved performance compared to NEB calculations^{42,43}. Additionally, it has been employed in a proof-of-principles study on ML-based path finding on low-dimensional potentials³². We note that an alternative approach is to formulate an implicit version of NEB by stopping the gradient in directions orthogonal to the current path, as proposed in concurrent work by Ramakrishnan et al.³³.

Given a dataset of paired reactant and product geometries, we transform the variational objective in Eq. (3) into a loss function for the parametrized reaction path by approximating the integral with Monte Carlo sampling over structures sampled from the predicted reaction path:

$$\mathcal{L}_{\text{flux}}(\theta) = \frac{1}{\beta} \log \mathbb{E}_{t \sim \mathcal{U}(0,1)} [\exp(\beta U(x_\theta(t))) \|\dot{x}_\theta(t)\|], \quad (5)$$

where $x_\theta(t) = f(x_R, x_P, a, t; \theta)$ denotes an image sampled from the parametrized reaction path.

Since Eq. (5) does not involve derivatives of U , computing its gradient $\nabla_\theta \mathcal{L}_{\text{flux}}(\theta)$ requires only first-order derivatives $\nabla_x U$, avoiding the need for Hessian evaluations. This makes the optimization process computationally efficient and compatible with a broad range of potential energy functions, including DFT, semiempirical quantum calculations, MLIPs, and classical force fields.

We additionally incorporate arc-length regularization³² to maintain a uniform distribution of points along the path. The regularization objec-

tive is designed to keep $\|\dot{x}(t)\|$ constant along the path, and defined as:

$$\begin{aligned}\mathcal{L}_{\text{arc}}[x(t)] &= \frac{1}{2} \int_0^1 \left(\partial_t \|\dot{x}(t)\|^2 \right)^2 dt \\ &= \int_0^1 \langle \dot{x}(t), \ddot{x}(t) \rangle^2 dt,\end{aligned}\quad (6)$$

$$\mathcal{L}_{\text{arc}}(\theta) = \mathbb{E}_{t \sim \mathcal{U}(0,1)} \left[\langle \dot{x}_\theta(t), \ddot{x}_\theta(t) \rangle^2 \right]. \quad (7)$$

Since Eqs. (3) and (5) are invariant under reparametrization of the interpolation parameter t , this additional objective helps to determine an appropriate curve parametrization. The final energy-based training loss function is a weighted sum of Eq. (5) and Eq. (7):

$$\mathcal{L}_{\text{energy}}(\theta) = \mathcal{L}_{\text{flux}}(\theta) + w_{\text{arc}} \mathcal{L}_{\text{arc}}(\theta), \quad (8)$$

with w_{arc} being a hyperparameter.

Geodesic initialization and pre-training

While linear interpolation is the simplest choice for the initial interpolation, it places the model far from the MEP, leading to high computational cost during energy-based training due to a large number of potential energy evaluations. In chain-of-states approaches, it is common to use informed initializations, such as image-dependent pair potentials (IDPP)⁴⁴ or geodesic interpolations⁴⁵, which provide fast, energy-free geometric optimization serving as a good initial guess for the MEP. We have also previously found that such interpolations provide a useful way to represent transition progress, serving as informative collective variables in the context of enhanced sampling⁴⁶. Similarly, we can accelerate reaction path training either by pre-training on geometric (energy-free) objective based on geodesic formalism to initialize the model closer to the MEP (MEPIN-L) or by directly using the geodesic path as the initial interpolation (MEPIN-G). This requires a differentiable geodesic path representation with respect to t , which we derive based on the geodesic interpolation method by Zhu et al.⁴⁵.

Geodesic interpolation is motivated by the differential geometry interpretation of intrinsic reaction coordinates (IRCs) by Tachibana and Fukui^{47,48}. In this framework, the metric tensor $\frac{\partial U}{\partial x^i} \frac{\partial U}{\partial x^j}$ redefines distance to effectively flatten the potential energy landscape, allowing the shortest path, i.e., the geodesic, to align with the MEP (Fig. 3a). To approximate this metric without explicitly using the potential energy U , Zhu et al.⁴⁵

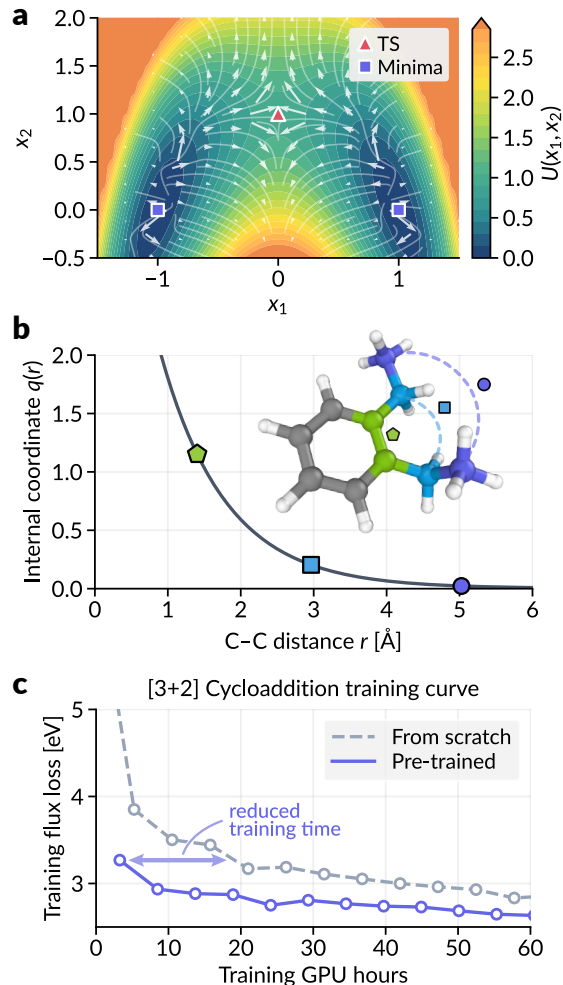


Figure 3: Geodesic interpolation. (a) Vectors with equal “length” under the metric $\frac{\partial U}{\partial x^1} \frac{\partial U}{\partial x^2}$, plotted on a two-dimensional potential $U(x^1, x^2)$. The length scale contracts compared to Cartesian coordinates as the position rises on the potential surface, making the MEP the shortest path on this metric. (b) Illustration of internal coordinates used to define the “length” in the geodesic interpolation scheme (Eq. (9)) for C-C interactions. Converting to internal coordinates prioritizes changes in bonded pairs over long-range non-bonded pairs. (c) Pre-training with geodesic loss (Eq. (11)) reduces the initial flux loss (Eq. (5)) significantly, accelerating the overall training time (including pre-training).

introduce a set of redundant internal coordinates q^k for each atomic pair $k = (m, n)$, representing pairwise interactions, defined as:

$$q^k = \exp \left(-\bar{\alpha} \frac{r_{mn} - r_{mn}^{\circ}}{r_{mn}^{\circ}} \right) + \bar{\beta} \frac{r_{mn}^{\circ}}{r_{mn}}, \quad (9)$$

where $r_{mn} = \|x_n - x_m\|$ is the interatomic distance, r_{mn}° is the sum of the covalent radii, and $\bar{\alpha} = 1.7$,

$\bar{\beta} = 0.01$ are hyperparameters controlling short- and long-range interactions. The infinitesimal distance element is defined through the induced metric tensor g_{ij} from the coordinate transformation:

$$ds^2 = g_{ij} dx^i dx^j = \frac{\partial q^k}{\partial x^i} \frac{\partial q^l}{\partial x^j} \delta_{kl} dx^i dx^j, \quad (10)$$

where Einstein summation notation is applied to sum over repeated indices in tensor expressions, and δ_{kl} denotes the Kronecker delta. The original geodesic interpolation is achieved by iteratively minimizing the length between the two endpoint geometries $\ell[x(t)] = \int_0^1 (g_{ij} \dot{x}^i(t) \dot{x}^j(t))^{1/2} dt = \int_0^1 \|\dot{q}(t)\| dt$ for a specified chain of images. As illustrated in Fig. 3b, the internal coordinates (Eq. (9)) effectively amplify changes in short-range distances, causing the geodesic path to avoid atomic clashes and follow a low-energy path.

We introduce two approaches inspired by this idea: (1) using the optimized geodesic path as the initial interpolation (MEPIN-**G**) or (2) using the linear initial interpolation but pre-training the path model with a geometric objective based on geodesic interpolation before energy-based training (MEPIN-**L**). This geometric pre-training moves the model closer to the MEP than random initialization, improving the efficiency of subsequent training. For the former, we generate the geodesic interpolation with a predefined number of images, and then represent the continuous initial interpolation $f_{\text{interp}}(x_R, x_P, a, t)$ in Eq. (1) as a cubic B-spline⁴⁹ with the geodesic images serving as control points. For the latter, we adapt the pre-training loss function to minimize the *geometric* energy, $\mathcal{E}[x(t)] = \frac{1}{2} \int_0^1 \|\dot{q}(t)\|^2 dt$, rather than the total curve length. This improves numerical stability while preserving the path shape. The corresponding geodesic loss for parameter optimization is then defined as:

$$\mathcal{L}_{\text{geodesic}}(\theta) = \mathbb{E}_{t \sim \mathcal{U}(0,1)} [\|\dot{q}_\theta(t)\|^2]. \quad (11)$$

We restrict the internal coordinate pairs in Eq. (9) to atom pairs within a predefined cutoff distance in the atomic graph.

In Fig. 3c, we demonstrate the efficiency gain of geodesic pre-training for MEPIN-**L** on the set of [3+2] cycloaddition reactions⁵⁰ used in our subsequent analysis. When plotting the flux loss (Eq. (5)) against the total training cost, we find that the model pre-trained with the geodesic loss starts from a much lower loss value than when trained from scratch, reducing the overall com-

putational cost. This shows that geodesic pre-training effectively aligns the reaction path model closer to the MEPs of the training reactions.

Reaction datasets To evaluate the proposed reaction path prediction approach, we created two reaction datasets derived from the Transition1x dataset³⁷ and the [3+2] cycloaddition reaction dataset⁵⁰. While the method is compatible with any potential energy function that provides gradients, we employed GFN1-xTB^{51,52} for computational efficiency. The Transition1x dataset³⁷, derived from Grambow et al.⁵³, was generated by enumerating possible elementary reactions between structures in the GDB7 dataset⁵⁴, which contains molecules with up to seven C, N, and O atoms (see example in Fig. 4a). The [3+2] cycloaddition dataset⁵⁰ consists of 1,3-dipolar cycloaddition reactions, as illustrated in Fig. 5a, featuring diverse dipoles, dipolarophiles, and their substituents. The Transition1x dataset contains small molecules with diverse reaction types and a wide range of activation barriers (Fig. 4b), while the cycloaddition dataset contains larger molecules with a single reaction type, differing in reactive moieties and substituents, with a narrower range of activation barriers (Fig. 5b).

We optimized the reactant and product complexes, as well as the transition states, at the GFN1-xTB level⁵¹. To ensure compatibility with the reaction path-finding model, we retained only reactions whose reactant and product complexes preserved molecular connectivity after GFN1-xTB optimization, ensuring they remain valid on the corresponding potential energy surface. After applying random train-test splits to these filtered datasets, we further refined the test set to include only reactions that remain unchanged on the GFN1-xTB potential energy surface with a workflow based on the SCINE framework^{55–61}. The verified subset of reactions includes only reactions with a transition state on the GFN1-xTB potential energy surface with only one imaginary frequency, and whose IRC connects to the optimized reactant and product complexes, as verified by SCINE MO-LASSEMBLER^{57,58}. We note that for training set reactions, we verified only the endpoints, without applying TS or IRC-based filtering, assuming such information is unavailable during training. The original TS structures in the Transition1x dataset³⁷ are also not IRC-verified, as they were obtained directly from climbing-image NEB (CI-NEB) calculations without further validation. Although TS

structures and NEB reaction paths were present in the original datasets, the path model was trained solely on reactant and product structures. Further details on dataset curation and training parameters can be found in the Supporting Information.

Transition1x reactions We trained two reaction path models, MEPIN-**L** and MEPIN-**G**, on a set of 8,069 reactions in the training and validation set, and evaluated the model on 316 reactions in the test set. For each reaction, we ran model inference with interpolation parameters $t = 0, 0.02, \dots, 1$ to yield 51 images along the predicted path. We compared this discretized path to the IRC connecting the same reactant and product. We measured the Fréchet distance⁶² between the reference path $x(t)$ and the prediction $\hat{x}(t)$, defined as

$$d_F[x, \hat{x}; \delta] = \min_{\gamma, \gamma'} \max_{t \in [0, 1]} \delta(x(\gamma(t)), \hat{x}(\gamma'(t))), \quad (12)$$

where $\gamma, \gamma' : [0, 1] \rightarrow [0, 1]$ are continuous, non-decreasing reparametrizations of t , and δ is a distance metric between two images. The Fréchet distance measures the minimum maximum distance required to traverse both paths while maintaining respective orderings, where distances between images are measured by a distance function δ . In this work, we use two different SE(3)-invariant δ : (1) the potential energy difference $\delta(x, y) = |U(x) - U(y)|$ and (2) the frame-aligned RMSD. Additionally, since the highest-energy configuration on the MEP should correspond to the TS, we compare the highest-energy image from the discretized predicted reaction path with the reference TS structure.

The results shown in Fig. 4c and Fig. 4d demonstrate that both reaction path models, MEPIN-**L** and MEPIN-**G**, outperform purely geometric interpolation methods in capturing the energetic profiles of reaction pathways, with lower discrete Fréchet distances based on energy and smaller TS energy deviations from the reference. The median deviations from the actual TS energies are 0.35 eV for MEPIN-**L** and 0.30 eV for MEPIN-**G**, indicating consistent and reliable identification of energetically aligned reaction paths and TSs across unseen reactions in the test set. Although the improvements in geometry, measured by RMSD, are less pronounced, both models still perform better than the baseline interpolations. The discrepancy between energetic and geometric alignment can be attributed to variations in molecular geometry that

have minimal impact on reaction energetics or multiple reactive pathways with similar activation energies, as illustrated in the example shown in Fig. S4. Hence, this behavior is likely due to the reaction path models being trained exclusively on energy-based objectives.

In most practical applications, the generated structures will still require optimization to confirm TS structures. Hence, we carried out saddle-point optimizations⁶³ of the predicted TSs generated by each interpolation method and reaction path model to evaluate whether the models offer improvements in both efficiency and accuracy for further refinement. As shown in Fig. S2, the TSs predicted by the reaction path models exhibit a higher matching rate with the reference TSs after optimization and require fewer optimization steps to converge to the saddle-point structure. This confirms that the reaction path models not only provide more accurate initial guesses but also enhance the overall computational efficiency of TS refinement workflows.

[3+2] cycloaddition reactions Similar to the Transition1x reaction set, we trained two reaction path models on 4,399 reactions from the training and validation set and evaluated them on 171 reactions in the test set. While we used the same evaluation metrics as before, RMSD-based comparisons were computed only over the five atoms that form the five-membered ring in the cycloadduct, allowing consistent geometric evaluation across reactants with varying substituent sizes. The results, shown in Fig. 5c and Fig. 5d, indicate that both models achieve again strong energetic alignment to the IRCs, with median TS energy deviations of 0.31 eV for MEPIN-**L** and 0.36 eV for MEPIN-**G**.

Unlike the results on Transition1x, MEPIN-**G** performs comparably to or worse than MEPIN-**L** in both energetic and geometric alignment for the [3+2] cycloaddition set. While explicitly optimized geodesic paths may be more beneficial for datasets with diverse reaction types, in cases like the [3+2] cycloaddition set—where reactions follow a consistent mechanistic motif—the pre-training and fine-tuning strategy of MEPIN-**L** appears sufficient to replace such initialization. In fact, the added curvature from geodesic-based paths may overly constrain the model, limiting its flexibility to adapt to patterns that can be learned directly from the data.

For the predicted TS structures, we again carried out saddle-point optimizations⁶³ to assess

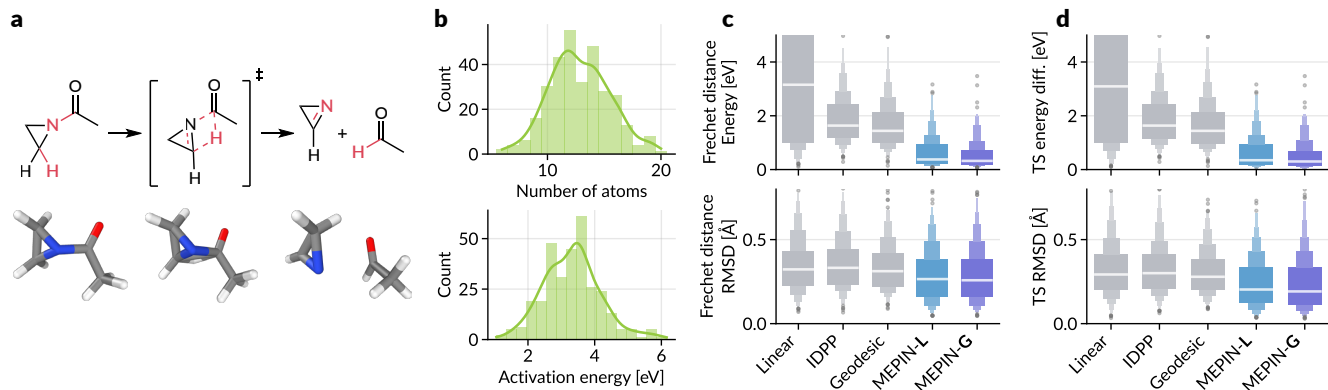


Figure 4: Results reaction path learning on the Transition1x reaction set³⁷. (a) Example reaction from the Transition1x dataset, comprising molecules with up to seven heavy atoms (C, N, O). (b) Distribution of atom count and reaction activation energy at the GFN1-xTB level⁵¹ for test set reactions. (c) Comparison of discrete Fréchet distance (Eq. (12)) to the IRC based on potential energy difference and RMSD of different interpolation methods and reaction path models (MEPIN-L and G). (d) Potential energy difference and RMSD between predicted and actual TS (highest energy configuration on the path), evaluated for various interpolation methods and reaction path models. The white horizontal lines represent median values.

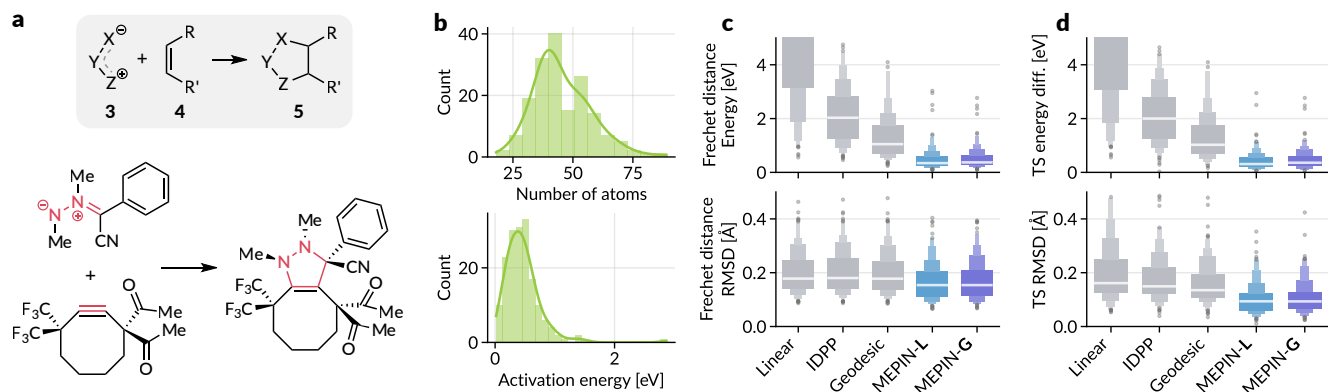


Figure 5: Results for reaction path learning on the [3+2] cycloaddition reaction set⁵⁰. (a) General reaction scheme for [3+2] cycloadditions, where dipole **3** and dipolarophile **4** undergo 1,3-cycloaddition to form cycloadduct **5**. An example reaction from the dataset is shown in the lower panel, with the reactive five-atom moieties highlighted. (b) Distribution of atom count and reaction activation energy at the GFN1-xTB level⁵¹ for test set reactions. (c) Comparison of discrete Fréchet distance (Eq. (12)) to the IRC based on energy difference and RMSD of different interpolation methods and reaction path models (MEPIN-L and G). (d) Energy difference and RMSD between predicted and actual TS (highest energy configuration on the path), evaluated for various interpolation methods and reaction path models. The white horizontal lines represent median values.

whether the model predictions improve computational efficiency in refinement workflows (Fig. S3). We similarly observed that learned reaction path models reduce the cost of TS refinement, with a notable increase in cases where the optimized TS matches the reference structure. Additionally, we analyzed the asynchronicity of the bond formation during the cycloaddition process to assess whether the predicted reaction paths capture chemical fea-

tures beyond geometric interpolation. Cycloaddition reactions proceed in a concerted yet asynchronous fashion, with the degree of asynchronicity influenced by the substituents and reactive moieties^{64,65}. To quantify this, we compared the differences in bond lengths for the two forming bonds at the predicted versus the reference TS structures. As illustrated in Fig. 6, the model predictions show much stronger correlations with refer-

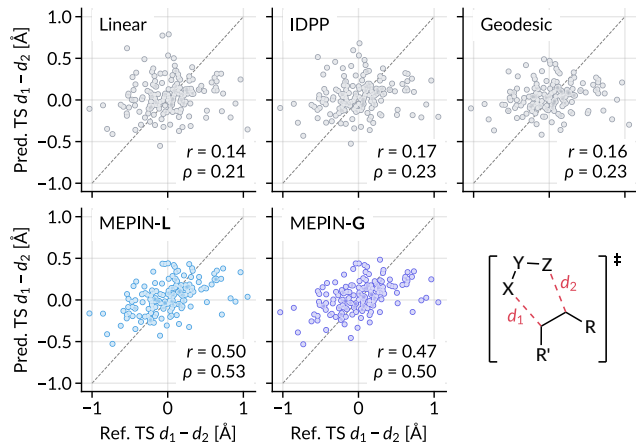


Figure 6: Probing the asynchronicity of the [3+2] cycloaddition with the reaction path model. For each interpolation method and reaction path model, the difference between the two forming bond distances at the TS (highest energy configuration) is compared to the reference TS for the test set reactions. Models trained with potential energy yield noticeably higher Pearson (r) and Spearman (ρ) correlations compared to purely geometric interpolation methods.

ence asynchronicity than geometric interpolations, indicating that the models learned to capture subtle, reaction-specific nuances and generalize across substituent variations.

Computational cost and comparison with previous methods The computational costs of the reaction path models (training and inference) and interpolation methods are provided in Supporting Information Section S3.3. Model inference takes less than 1 ms on a GPU and 10–30 ms on a CPU per predicted image, comparable to or faster than interpolation methods based on geometric optimization (e.g., IDPP and geodesic). Although training involves a few hundred energy and force evaluations per reaction, it does not require pre-optimized TSs or reaction paths, and inference requires no energy evaluations.

While there were no prior works on transferable prediction of entire reaction paths, recent studies on ML-based transition characterization have focused on directly predicting TS structures^{22–26} or pre-computed reaction energetics^{66,67}. These approaches depend on large datasets of TS structures generated via computationally intensive methods like CI-NEB, which are challenging to automate and prone to failure. Additionally, they typically yield only a single TS structure or activation en-

ergy per inference, limiting their application to broad, mechanism-free reaction discovery. In contrast, our method eliminates the need for explicit TS annotations by training exclusively on endpoint structures with energy-based supervision, enabling the generation of full reaction paths that can be discretized as needed. This makes our approach well-suited for integration into automated reaction enumeration and exploration pipelines.^{68–75}

Some of the aforementioned works reported strong performance on specific datasets—for example, Duan et al.²⁵ report ~ 0.075 Å RMSD for TS structure reproduction in the Transition1x dataset³⁷. However, such metrics may not reflect the success in recovering the correct path information, as the TS structures in the dataset are derived directly from CI-NEB calculations and are not verified by IRC calculations. Thus, the modeling approach should be selected based on the desired prediction outcome and the availability of prior transition path or structure data.

Conclusion We have introduced MEPIN, an efficient and scalable reaction path modeling approach that accelerates the identification of MEPS without requiring prior knowledge of TS structures during training. By combining a parametrized reaction path model with an energy-based training objective and a geodesic initialization or pre-training strategy, our approach achieves accurate energetic alignment with reference IRCs across diverse reaction types. Evaluations on both the Transition1x and [3+2] cycloaddition reaction sets demonstrate generalization to unseen reaction pathways and features. Future work could improve this approach by exploring transfer learning or multi-fidelity strategies across multiple potential energy surfaces to leverage high-accuracy DFT-level data⁷⁶. In addition, incorporating generative modeling to discover multiple possible reaction pathways⁷⁷ would be crucial, as reactions can proceed via alternative routes that are not captured by current single-path modeling strategies. Furthermore, multi-objective learning methods⁷⁸ that additionally integrate available TS or optimized reaction path data could further improve geometric accuracy and performance, addressing the current limitations of our model compared to methods explicitly trained on known TS structures or reaction paths.

Data availability The code and data to reproduce the results of this work have been made

available on GitHub: <https://github.com/learningmatter-mit/mepin>.

Acknowledgement The authors thank Xiaochen Du for carefully reviewing the manuscript and providing valuable suggestions, and Minh Kim, MinGyu Choi, and Luigi Bonati for insightful discussions. This research used resources of the National Energy Research Scientific Computing Center (NERSC), a Department of Energy Office of Science User Facility using NERSC awards BES-ERCAP-m4737 and BES-ERCAP-m4866. We also acknowledge the MIT SuperCloud and Lincoln Laboratory Supercomputing Center for providing HPC resources. J.N. was supported by the Energy Storage Research Alliance “ESRA” (DE-AC02-06CH11357), an Energy Innovation Hub funded by the U.S. Department of Energy, Office of Science, Basic Energy Sciences. M.S. gratefully acknowledges the Mobility fellowship P500PN.225736 from the Swiss National Science Foundation. M.M. was supported by the MIT Undergraduate Research Opportunities Program. A.S. acknowledges support from the National Defense Science and Engineering Graduate Fellowship.

Supporting Information Available

Details on model architecture, training procedures, and hyperparameters; dataset preparation and comparison with the original dataset; and additional results, including saddle-point optimization, inference examples, and computational cost.

References

- (1) Mills, G.; Jónsson, H.; Schenter, G. K. Reversible work transition state theory: application to dissociative adsorption of hydrogen. *Surf. Sci.* **1995**, *324*, 305–337.
- (2) Jónsson, H.; Mills, G.; Jacobsen, K. W. *Classical and quantum dynamics in condensed phase simulations*; World Scientific, 1998; pp 385–404.
- (3) Henkelman, G.; Jónsson, H. Improved tangent estimate in the nudged elastic band method for finding minimum energy paths and saddle points. *J. Chem. Phys.* **2000**, *113*, 9978–9985.
- (4) Trygubenko, S. A.; Wales, D. J. A doubly nudged elastic band method for finding transition states. *J. Chem. Phys.* **2004**, *120*, 2082–2094.
- (5) Sheppard, D.; Terrell, R.; Henkelman, G. Optimization methods for finding minimum energy paths. *J. Chem. Phys.* **2008**, *128*.
- (6) Yang, Y.; Zhang, S.; Ranasinghe, K. D.; Isayev, O.; Roitberg, A. E. Machine learning of reactive potentials. *Annu. Rev. Phys. Chem.* **2024**, *75*, 371–395.
- (7) Zhang, S.; Makoś, M. Z.; Jadrich, R. B.; Kraka, E.; Barros, K.; Nebgen, B. T.; Tretiak, S.; Isayev, O.; Lubbers, N.; Messerly, R. A. et al. Exploring the frontiers of condensed-phase chemistry with a general reactive machine learning potential. *Nat. Chem.* **2024**, *16*, 727–734.
- (8) Schreiner, M.; Bhowmik, A.; Vegge, T.; Jørgensen, P. B.; Winther, O. Neural-NEB—neural networks can find reaction paths fast. *Mach. Learn.: Sci. Technol.* **2022**, *3*, 045022.
- (9) Wander, B.; Shuaibi, M.; Kitchin, J. R.; Ulissi, Z. W.; Zitnick, C. L. CatTSunami: Accelerating Transition State Energy Calculations with Pre-trained Graph Neural Networks. 2024; <https://arxiv.org/abs/2405.02078>.
- (10) Yuan, E. C.-Y.; Kumar, A.; Guan, X.; Hermes, E. D.; Rosen, A. S.; Zádor, J.; Head-Gordon, T.; Blau, S. M. Analytical ab initio hessian from a deep learning potential for transition state optimization. *Nat. Commun.* **2024**, *15*, 8865.
- (11) Marks, J.; Gomes, J. Efficient Transition State Searches by Freezing String Method with Graph Neural Network Potentials. 2025; <https://arxiv.org/abs/2501.06159>.
- (12) Anstine, D.; Zubatyuk, R.; Gallegos, L.; Patton, R.; Wiest, O.; Nebgen, B.; Jones, T.; Gomes, G.; Tretiak, S.; Isayev, O. Transferable Machine Learning Interatomic Potential for Pd-Catalyzed Cross-Coupling Reactions. 2025; <https://doi.org/10.26434/chemrxiv-2025-n36r6>.

- (13) Käser, S.; Unke, O. T.; Meuwly, M. Reactive dynamics and spectroscopy of hydrogen transfer from neural network-based reactive potential energy surfaces. *New J. Phys.* **2020**, *22*, 055002.
- (14) Ang, S. J.; Wang, W.; Schwalbe-Koda, D.; Axelrod, S.; Gómez-Bombarelli, R. Active learning accelerates ab initio molecular dynamics on reactive energy surfaces. *Chem* **2021**, *7*, 738–751.
- (15) Li, J.; Stein, R.; Adrion, D. M.; Lopez, S. A. Machine-Learning Photodynamics Simulations Uncover the Role of Substituent Effects on the Photochemical Formation of Cubanes. *J. Am. Chem. Soc.* **2021**, *143*, 20166–20175.
- (16) Westermayr, J.; Gastegger, M.; Vörös, D.; Panzenboeck, L.; Joerg, F.; González, L.; Marquetand, P. Deep learning study of tyrosine reveals that roaming can lead to photodamage. *Nat. Chem.* **2022**, *14*, 914–919.
- (17) A. Young, T.; Johnston-Wood, T.; L. Deringer, V.; Duarte, F. A transferable active-learning strategy for reactive molecular force fields. *Chem. Sci.* **2021**, *12*, 10944–10955.
- (18) A. Young, T.; Johnston-Wood, T.; Zhang, H.; Duarte, F. Reaction dynamics of Diels–Alder reactions from machine learned potentials. *Phys. Chem. Chem. Phys.* **2022**, *24*, 20820–20827.
- (19) Yang, M.; Bonati, L.; Polino, D.; Parrinello, M. Using metadynamics to build neural network potentials for reactive events: the case of urea decomposition in water. *Catal. Today* **2022**, *387*, 143–149.
- (20) Célerse, F.; Juraskova, V.; Das, S.; Wodrich, M. D.; Corminboeuf, C. Capturing Dichotomic Solvent Behavior in Solute–Solvent Reactions with Neural Network Potentials. *J. Chem. Theory Comput.* **2024**, *20*, 10350–10361.
- (21) Zhang, H.; Juraskova, V.; Duarte, F. Modelling chemical processes in explicit solvents with machine learning potentials. *Nat. Commun.* **2024**, *15*, 6114.
- (22) Choi, S. Prediction of transition state structures of gas-phase chemical reactions via machine learning. *Nat. Commun.* **2023**, *14*, 1168.
- (23) Duan, C.; Du, Y.; Jia, H.; Kulik, H. J. Accurate transition state generation with an object-aware equivariant elementary reaction diffusion model. *Nat. Comput. Sci.* **2023**, *3*, 1045–1055.
- (24) Kim, S.; Woo, J.; Kim, W. Y. Diffusion-based generative AI for exploring transition states from 2D molecular graphs. *Nat. Commun.* **2024**, *15*, 341.
- (25) Duan, C.; Liu, G.-H.; Du, Y.; Chen, T.; Zhao, Q.; Jia, H.; Gomes, C. P.; Theodorou, E. A.; Kulik, H. J. React-OT: Optimal Transport for Generating Transition State in Chemical Reactions. 2024; <https://arxiv.org/abs/2404.13430>.
- (26) Zhao, Q.; Han, Y.; Zhang, D.; Wang, J.; Zhong, P.; Cui, T.; Yin, B.; Cao, Y.; Jia, H.; Duan, C. Harnessing Machine Learning to Enhance Transition State Search with Interatomic Potentials and Generative Models. **2025**,
- (27) Kang, P.; Trizio, E.; Parrinello, M. Computing the committor with the committor to study the transition state ensemble. *Nat. Comput. Sci.* **2024**, *4*, 451–460.
- (28) Singh, A. N.; Limmer, D. T. Splitting probabilities as optimal controllers of rare reactive events. *J. Chem. Phys.* **2024**, *161*.
- (29) Du, Y.; Plainer, M.; Brekelmans, R.; Duan, C.; Noe, F.; Gomes, C. P.; Aspuru-Guzik, A.; Neklyudov, K. Doob’s Lagrangian: A Sample-Efficient Variational Approach to Transition Path Sampling. The Thirty-eighth Annual Conference on Neural Information Processing Systems. 2024.
- (30) Wang, H.; Qiu, Y.; Wang, Y.; Brekelmans, R.; Du, Y. Generalized Flow Matching for Transition Dynamics Modeling. *arXiv preprint arXiv:2410.15128* **2024**,
- (31) Seong, K.; Park, S.; Kim, S.; Kim, W. Y.; Ahn, S. Transition Path Sampling with Improved Off-Policy Training of Diffusion Path Samplers. 2025; <https://arxiv.org/abs/2405.19961>.
- (32) Han, J.; Gu, S.; Zhou, X. StringNET: Neural Network based Variational Method for Transition Pathways. 2024; <https://arxiv.org/abs/2408.12621>.

- (33) Ramakrishnan, K.; Schaaf, L. L.; Lin, C.; Wang, G.; Torr, P. Implicit Neural Representations for Chemical Reaction Paths. 2025; <https://arxiv.org/abs/2502.15843>.
- (34) Blau, S.; Hegazy, K.; Yuan, E.; Kumar, A.; Mahoney, M.; Head-Gordon, T. Neural network path optimization for finding transition states on a machine learned potential. ACS Spring 2025, San Diego, CA, USA.
- (35) Schütt, K.; Unke, O.; Gastegger, M. Equivariant message passing for the prediction of tensorial properties and molecular spectra. Proceedings of the 38th International Conference on Machine Learning. 2021; pp 9377–9388.
- (36) VanLeeuwen, B. K.; Gopalan, V. The antisymmetry of distortions. *Nat. Commun.* **2015**, *6*, 8818.
- (37) Schreiner, M.; Bhowmik, A.; Vegge, T.; Busk, J.; Winther, O. Transition1x-a dataset for building generalizable reactive machine learning potentials. *Sci. Data* **2022**, *9*, 779.
- (38) Schreiner, M.; Winther, O.; Olsson, S. Implicit Transfer Operator Learning: Multiple Time-Resolution Models for Molecular Dynamics. Advances in Neural Information Processing Systems. 2023; pp 36449–36462.
- (39) Xie, Y.; Smidt, T. Equivariant Symmetry Breaking Sets. *Trans. Mach. Learn. Res.* **2024**,
- (40) Berkowitz, M.; Morgan, J.; McCammon, J.; Northrup, S. Diffusion-controlled reactions: A variational formula for the optimum reaction coordinate. *J. Chem. Phys.* **1983**, *79*, 5563.
- (41) Huo, S.; Straub, J. E. The MaxFlux algorithm for calculating variationally optimized reaction paths for conformational transitions in many body systems at finite temperature. *J. Chem. Phys.* **1997**, *107*, 5000–5006.
- (42) Koda, S.-i.; Saito, S. Flat-Bottom Elastic Network Model for Generating Improved Plausible Reaction Paths. *J. Chem. Theory Comput.* **2024**, *20*, 7176–7187.
- (43) Koda, S.-i.; Saito, S. Locating Transition States by Variational Reaction Path Optimization with an Energy-Derivative-Free Objective Function. *J. Chem. Theory. Comput.* **2024**, *20*, 2798–2811.
- (44) Smidstrup, S.; Pedersen, A.; Stokbro, K.; Jónsson, H. Improved initial guess for minimum energy path calculations. *J. Chem. Phys.* **2014**, *140*.
- (45) Zhu, X.; Thompson, K. C.; Martínez, T. J. Geodesic interpolation for reaction pathways. *J. Chem. Phys.* **2019**, *150*.
- (46) Yang, S.; Nam, J.; Dietschreit, J. C.; Gómez-Bombarelli, R. Learning collective variables with synthetic data augmentation through physics-inspired geodesic interpolation. *J. Chem. Theory Comput.* **2024**, *20*, 6559–6568.
- (47) Tachibana, A.; Fukui, K. Differential geometry of chemically reacting systems. *Theor. Chim. Acta* **1978**, *49*, 321–347.
- (48) Tachibana, A.; Fukui, K. Intrinsic field theory of chemical reactions. *Theor. Chim. Acta* **1979**, *51*, 275–296.
- (49) Bartels, R. H.; Beatty, J. C.; Barsky, B. A. *An introduction to splines for use in computer graphics and geometric modeling*; Morgan Kaufmann, 1995.
- (50) Stuyver, T.; Jorner, K.; Coley, C. W. Reaction profiles for quantum chemistry-computed [3+2] cycloaddition reactions. *Sci. Data* **2023**, *10*, 66.
- (51) Grimme, S.; Bannwarth, C.; Shushkov, P. A robust and accurate tight-binding quantum chemical method for structures, vibrational frequencies, and noncovalent interactions of large molecular systems parametrized for all spd-block elements (Z=1–86). *J. Chem. Theory Comput.* **2017**, *13*, 1989–2009.
- (52) Friede, M.; Hölzer, C.; Ehlert, S.; Grimme, S. dxtb—An efficient and fully differentiable framework for extended tight-binding. *J. Chem. Phys.* **2024**, *161*.
- (53) Grambow, C. A.; Pattanaik, L.; Green, W. H. Reactants, products, and transition states of elementary chemical reactions based on quantum chemistry. *Sci. Data* **2020**, *7*, 137.

- (54) Ruddigkeit, L.; Van Deursen, R.; Blum, L. C.; Reymond, J.-L. Enumeration of 166 billion organic small molecules in the chemical universe database GDB-17. *J. Chem. Inf. Model.* **2012**, *52*, 2864–2875.
- (55) Weymuth, T.; Unsleber, J. P.; Türtcher, P. L.; Steiner, M.; Sobez, J.-G.; Müller, C. H.; Mörchen, M.; Klasovita, V.; Grimm, S. A.; Eckhoff, M. et al. SCINE – Software for chemical interaction networks. *J. Chem. Phys.* **2024**, *160*, 222501.
- (56) Vaucher, A. C.; Reiher, M. Minimum Energy Paths and Transition States by Curve Optimization. *J. Chem. Theory Comput.* **2018**, *14*, 3091–3099.
- (57) Sobez, J.-G.; Reiher, M. Molassembler: Molecular Graph Construction, Modification, and Conformer Generation for Inorganic and Organic Molecules. *J. Chem. Inf. Model.* **2020**, *60*, 3884–3900.
- (58) Bensberg, M.; Grimm, S.; Sobez, J.-G.; Steiner, M.; Unsleber, J. P.; Reiher, M. qcscine/molassembler: Release 3.0.0. 2024; <https://doi.org/10.5281/zenodo.13372940>.
- (59) Bensberg, M.; Brunken, C.; Csizi, K.-S.; Grimm, S. A.; Gugler, S.; Sobez, J.-G.; Steiner, M.; Türtcher, P. L.; Unsleber, J. P.; Vaucher, A. et al. qcscine/readuct: Release 6.0.0. 2024; <https://doi.org/10.5281/zenodo.13372944>.
- (60) Bensberg, M.; Csizi, K.-S.; Grimm, S. A.; Sobez, J.-G.; Steiner, M.; Türtcher, P. L.; Unsleber, J. P.; Reiher, M. qcscine/xtb-wrapper: Release 3.0.1. 2024; <https://doi.org/10.5281/zenodo.13372943>.
- (61) Baiardi, A.; Bensberg, M.; Bosia, F.; Brunken, C.; Csizi, K.-S.; Feldmann, R.; Glaser, N.; Grimm, S. A.; Gugler, S.; Haag, M. et al. qcscine/utilities: Release 10.0.0. 2024; <https://doi.org/10.5281/zenodo.13372905>.
- (62) Eiter, T.; Mannila, H. Computing discrete Fréchet distance. **1994**,
- (63) Hermes, E. D.; Sargsyan, K.; Najm, H. N.; Zádor, J. Sella, an open-source automation-friendly molecular saddle point optimizer. *J. Chem. Theory Comput.* **2022**, *18*, 6974–6988.
- (64) Barrales-Martínez, C.; Martínez-Araya, J. I.; Jaque, P. 1,3-Dipolar cycloadditions by a unified perspective based on conceptual and thermodynamics models of chemical reactivity. *J. Phys. Chem. A* **2021**, *125*, 801–815.
- (65) Kawamura, M. Y.; Alegre-Requena, J. V.; Barbosa, T. M.; Tormena, C. F.; Paton, R. S.; Ferreira, M. A. Mechanistic Aspects on [3+2] Cycloaddition (32CA) Reactions of Azides to Nitroolefins: A Computational and Kinetic Study. *Chem. Eur. J.* **2022**, *28*, e202202294.
- (66) van Gerwen, P.; Fabrizio, A.; Wodrich, M. D.; Corminboeuf, C. Physics-based representations for machine learning properties of chemical reactions. *Mach. Learn.: Sci. Technol.* **2022**, *3*, 045005.
- (67) van Gerwen, P.; Briling, K. R.; Bunne, C.; Somnath, V. R.; Laplaza, R.; Krause, A.; Corminboeuf, C. 3DReact: Geometric deep learning for chemical reactions. *J. Chem. Inf. Model.* **2024**, *64*, 5771–5785.
- (68) Dewyer, A. L.; Argüelles, A. J.; Zimmerman, P. M. Methods for Exploring Reaction Space in Molecular Systems. *WIREs Comput. Mol. Sci.* **2018**, *8*, e1354.
- (69) Simm, G. N.; Vaucher, A. C.; Reiher, M. Exploration of Reaction Pathways and Chemical Transformation Networks. *J. Phys. Chem. A* **2019**, *123*, 385–399.
- (70) Unsleber, J. P.; Reiher, M. The Exploration of Chemical Reaction Networks. *Annu. Rev. Phys. Chem.* **2020**, *71*, 121–142.
- (71) Baiardi, A.; Grimm, S. A.; Steiner, M.; Türtcher, P. L.; Unsleber, J. P.; Weymuth, T.; Reiher, M. Expansive Quantum Mechanical Exploration of Chemical Reaction Paths. *Acc. Chem. Res.* **2022**, *55*, 35–43.
- (72) Ismail, I.; Majerus, R. C.; Habershon, S. Graph-Driven Reaction Discovery: Progress, Challenges, and Future Opportunities. *J. Phys. Chem. A* **2022**, *126*, 7051–7069.

- (73) Wen, M.; Spotte-Smith, E. W. C.; Blau, S. M.; McDermott, M. J.; Krishnapriyan, A. S.; Persson, K. A. Chemical reaction networks and opportunities for machine learning. *Nat. Comput. Sci.* **2023**, *3*, 12–24.
- (74) Margraf, J. T.; Jung, H.; Scheurer, C.; Reuter, K. Exploring Catalytic Reaction Networks with Machine Learning. *Nat. Catal.* **2023**, *6*, 112–121.
- (75) Steiner, M.; Reiher, M. Autonomous Reaction Network Exploration in Homogeneous and Heterogeneous Catalysis. *Top. Catal.* **2022**, *65*, 6–39.
- (76) Greenman, K. P.; Green, W. H.; Gómez-Bombarelli, R. Multi-fidelity prediction of molecular optical peaks with deep learning. *Chem. Sci.* **2022**, *13*, 1152–1162.
- (77) Hayashi, A.; Takamoto, S.; Li, J.; Tsuboi, Y.; Okanohara, D. Generative Model for Constructing Reaction Path from Initial to Final States. *J. Chem. Theory Comput.* **2024**,
- (78) Bonati, L.; Trizio, E.; Rizzi, A.; Parrinello, M. A unified framework for machine learning collective variables for enhanced sampling simulations: mlcolvar. *J. Chem. Phys.* **2023**, *159*.